Mon. Not. R. Astron. Soc. **324,** 1117–1130 (2001)

100-yr mass-loss modulations on the asymptotic giant branch

Massimo Marengo,[1,2]★ Željko Ivezić[3]★ and Gillian R. Knapp[3]★
[1]*Harvard-Smithsonian Center for Astrophysics, Cambridge, MA 02138, USA*
[2]*International School for Advanced Studies, SISSA/ISAS, Trieste, Italy*
[3]*Princeton University, Department of Astrophysical Sciences, Princeton, NJ 08544, USA*

Accepted 2001 February 7. Received 2001 February 1; in original form 2000 October 3

Downloaded from https://academic.oup.com/mnras/article/324/4/1117/1316774 by guest on 21 August 2022

ABSTRACT

We analyse the differences in infrared circumstellar dust emission between oxygen-rich Mira and non-Mira stars, and find that they are statistically significant. In particular, we find that these stars segregate in the K–[12] versus [12]–[25] colour–colour diagram, and have distinct properties of the *IRAS* LRS spectra, including the peak position of the silicate emission feature. We show that the infrared emission from the majority of non-Mira stars cannot be explained within the context of standard steady-state outflow models.

The models can be altered to fit the data for non-Mira stars by postulating non-standard optical properties for silicate grains, or by assuming that the dust temperature at the inner envelope radius is significantly lower (300–400 K) than typical silicate grain condensation temperatures (800–1000 K). We argue that the latter is more probable and provide detailed model fits to the *IRAS* LRS spectra for 342 stars. These fits imply that two-thirds of non-Mira stars and one-third of Mira stars do not have hot dust ($>$500 K) in their envelopes.

The absence of hot dust can be interpreted as a recent ($\sim$100 yr) decrease in the mass-loss rate. The distribution of best-fitting model parameters agrees with this interpretation and strongly suggests that the mass loss resumes on similar time-scales. Such a possibility appears to be supported by a number of spatially resolved observations (e.g. recent *Hubble Space Telescope* images of the multiple shells in the Egg Nebula) and is consistent with new dynamical models for mass loss on the asymptotic giant branch.

Key words: stars: AGB and post-AGB – circumstellar matter – stars: mass-loss – stars: variables: other – infrared: stars.

1 INTRODUCTION

Asymptotic giant branch (AGB) stars are surrounded by dusty shells that emit copious infrared radiation. Even before the *IRAS* data became available, it was shown that infrared (IR) spectra of AGB stars can be reasonably well modelled by thermal emission from dust with a radial density distribution $\propto r^{-2}$, and optical properties for either silicate, or carbonaceous grains (Rowan-Robinson & Harris 1982, 1983a,b). The availability of four *IRAS* broad-band fluxes and the *IRAS* LRS data base for thousands of objects made possible more detailed statistical studies. Van der Veen & Habing (1988) found that AGB stars occupy a well-defined region in the *IRAS* 12–25–60 colour–colour diagram. They also showed that the source distribution depends on the grain chemistry, and is correlated with the LRS spectral classification. Bedijn (1987) showed that in addition to grain chemistry, the most important quantity that determines the position of a particular source in the *IRAS* 12–25–60 colour–colour diagram is its mass-loss rate: more dust, more IR emission.

A dust density distribution $\propto r^{-2}$ is expected for a spherical outflow at constant velocity. Since typical observed velocities are much larger than the estimated escape velocities, there must be an acceleration mechanism at work. Early studies by Gilman (1969) and Salpeter (1974a,b), and later by others (e.g. Netzer & Elitzur 1993; Habing, Tignon & Tielens 1994), showed that the luminosity-to-mass ratios for AGB stars are sufficiently large to permit outflows driven by radiation pressure. In this model, hereafter called 'standard', the dust acceleration is significant only close to the inner envelope edge, and thus the dust density is steeper than r^{-2} only at radii smaller than about several r_1. Here r_1 is the inner envelope radius that corresponds to the dust condensation point. At larger radii the dust density closely follows the r^{-2} law, in agreement with the observed mid- and far-IR emission. In particular, Ivezić & Elitzur (1995; hereafter IE95) find that such steady-state radiation-pressure-driven outflow models can explain the *IRAS* colours for at least 95 per cent of dusty AGB stars. In addition to explaining the IR emission, these models are in good agreement with constraints implied by independent outflow

★E-mail: mmarengo@cfa.harvard.edu (MM); ivezic@astro.princeton.edu (ZI); gk@astro.princeton.edu (GRK)

© 2001 RAS

velocity and mass-loss rate measurements (Ivezić, Knapp & Elitzur 1998).

AGB stars are long-period variables (LPV) which show a variety of light curves. Based on visual light curves, the General Catalogue of Variable Stars (GCVS, Kholopov et al. 1985–88) defines regular variables, or Miras, semiregular (SR) variables, and irregular variables (L). The distinctive features are the regularity of the light curves, their amplitudes, and their periods. Some types are further subdivided based on similar criteria (e.g. SRa, SRb, SRc, etc.).

AGB stars of different variability types cannot be distinguished in *IRAS* colour–colour diagrams (Habing 1996 and references therein). This is easily understood as a consequence of the scaling properties of dust emission (IE95; Ivezić & Elitzur 1997; hereafter IE97). Although steady-state models cannot provide a detailed description of variability, they can be easily augmented when the variability time-scale ($\sim$1 yr) is shorter than the dust dynamical crossing time through the acceleration zone ($>$10 yr). In this case the deviations of the dust density profile are minor, and the most important effect of variability is the change of dust optical depth. Optical depth is anticorrelated with luminosity because of the movement of the dust condensation point: envelopes are bluer (in all colours) during maximum than minimum light (Le Bertre 1988a,b; Ivezić & Elitzur 1996 and references therein). Since the change of dust density profile is negligible, a source cannot leave the track in colour–colour diagrams that corresponds to that density profile and grain chemistry: during its variability cycle the source simply moves along that track due to the change of optical depth. Consequently, the overall source distribution is not significantly affected and a random observation cannot reveal any peculiarities: even if a star is caught during its maximum/minimum light, the only change is in its somewhat bluer/redder colours [see, e.g., the repeated observations of Mira by Busso et al. (1996)]. For this reason, systematic differences in *IRAS* colour–colour diagrams for AGB stars of different variability types are not expected within the framework of steady-state models.

Kerschbaum, Hron and collaborators (Kerschbaum & Hron 1992; 1994, 1996; Kerschbaum, Olofsson & Hron 1996; Hron, Aringer & Kerschbaum 1997; hereafter we refer to these papers as KHc) studied IR emission of various types of LPVs by combining the *IRAS* broad-band fluxes with near-IR observations and the *IRAS* LRS data base. They find differences in observed properties between Miras and SRb/Lb variables[1]: SRb/Lb variables have somewhat higher stellar temperatures and smaller optical depths than Miras, and can be further divided into 'blue' and 'red' subtypes, the former showing much less evidence for dust emission than the latter. KHc also show that 'red' SRb/Lb stars have very similar Galactic scaleheights and space densities to Miras, and show a similar range of *IRAS* 25–12 colour, possibly implying an evolutionary connection.

Particularly intriguing are differences between the LRS spectra of SRb/Lb variables and Miras with '9.7-μm' silicate emission (LRS Class 2n). Unlike the featureless spectra of carbonaceous grains, the silicate dust spectra show rich structure (e.g. Little-Marenin & Little 1988, 1990). This structure may indicate the existence of different dust species, although some of the proposed classification appears to reflect the radiative transfer effects (IE95). The peak position of the '9.7-μm' feature for SRb/Lb sources is shifted longwards, relative to the peak position for Miras, by 0.2–0.3 μm. In addition, the ratio of the strengths of silicate emission features at 18 and 10 μm, $F_{18}F_{10}$, is larger for SRb/Lb variables than for Miras. KHc point out that these differences in LRS features cannot be caused by optical depth effects because the feature shapes should resemble the grain absorption efficiency for the relevant range of optical depths. Such a correlation between the variability type of a star and the peak position of its grain absorption efficiency is not expected within the context of standard steady-state outflow models.

Ivezić & Knapp (1998; hereafter IK98) compared the distribution of variable AGB stars in the K–[12] versus [12]–[25] colour–colour diagram and found that stars are not distributed randomly in this diagram, but occupy well-defined regions according to their chemistry and variability type. While discrimination according to the chemical composition is not surprising, since the optical properties of silicate and carbon grains are significantly different, the separation of Miras from SRb/Lb variables is unexpected.

IK98 also show that, while 'standard' steady-state models provide excellent fits to the distributions of Miras of all chemical types, they are incapable of explaining the dust emission from SRb/Lb stars with silicate dust. They find that the distribution of these stars in the K–[12] versus [12]–[25] colour–colour diagram can be explained by models with dust temperature at the inner envelope radius significantly lower (300–400 K) than typical condensation temperatures (800–1000 K). Such an absence of hot dust for SRb/Lb stars can be interpreted as a recent (order of 100 yr) decrease in the mass-loss rate. Furthermore, the distribution of these stars in the K–[12] versus [12]–[25] colour–colour diagram implies that the mass-loss rate probably resumes again, on similar time-scales.

The possibility of mass loss changes with short time-scales (of the order of 100 yr) seems to be supported by a number of other observations. Recent *Hubble Space Telescope* (*HST*) images of the Egg Nebula obtained by Sahai et al. (1999) show concentric shells, the spacing of which corresponds to a dynamical time-scale of about 100 yr. Although there are various ways to interpret such shells [e.g. a binary companion as proposed by Harpaz, Rappaport & Soker (1997); instabilities in the dust-gas coupling proposed by Deguchi (1997)], another possible explanation is dust density modulations owing to the mass-loss variations on similar time-scales. Time-scales of $\sim$100 yr for mass-loss variations have also been inferred for R Hya by Hashimoto et al. (1998) and for IRC+10216 by Mauron & Huggins (1999), and a somewhat longer scale for μ Cep by Mauron (1997). The discovery of multiple CO winds reported by Knapp et al. (1998) is also in agreement with the hypothesis of variable mass loss.

Mass-loss rate modulations with time-scales of the order of 100 yr are difficult to explain in terms of the periodicities characteristic for AGB stars. Periodic flashes of the He burning shell in the thermally pulsing AGB phase (known as 'thermal pulses', TP hereafter) occur on time-scales of 10^3–10^4 yr (see, e.g., Speck, Meixner & Knapp 2000). On the other end, the typical pulsational periods of AGB stars (50–500 d) are too short. Various attempts to solve this puzzle have been proposed, and are well described by Sahai et al. (1999). The basic ideas involve either long-period modulations of the luminosity variations, or temperature fluctuations caused by giant convection cells in the AGB atmosphere. However, similar mass-loss rate modulations are also reproduced, without any such additional assumptions, within the framework of time-dependent wind models with the driving force varying on time-scales of $\sim$1 yr (Winters 1998, see also Section 4).

[1] According to KHc, SRa variables appear to be a mixture of two distinct types: Miras and SRb variables.

Downloaded from https://academic.oup.com/mnras/article/324/4/1117/1316774 by guest on 21 August 2022

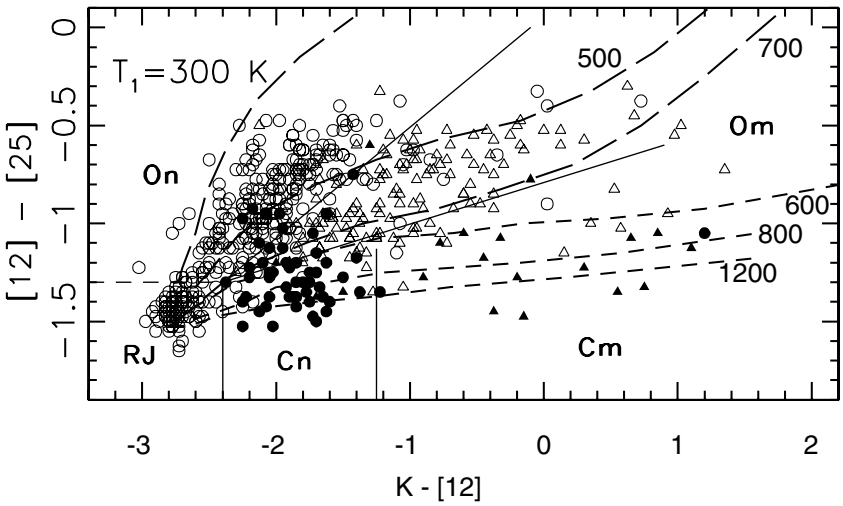

Figure 1. [12]–[25] versus K–[12] colour–colour diagram for a sample of AGB stars discussed in IK98. Oxygen-rich Miras and SRb/Lb stars are marked by open triangles and circles, respectively. Carbon rich stars are analogously marked by full symbols. The thin straight full curves display a scheme which classifies stars into 4 groups according to their variability type (Miras, m, versus non-Miras, n) and chemistry (O versus C). The RJ label marks the locus of dust-free stars. The thick curved short-dashed and long-dashed curves represent tracks for interrupted mass-loss models which are described in detail in Section 3. It is assumed that mass loss abruptly stops and the envelope freely expands thereafter. Note that the models imply a lack of hot dust for oxygen-rich SRb/Lb stars.

Motivated by these results, we further analyse correlations between variability type and IR emission for AGB stars, especially the properties of LRS data, and their implications for the models of steady-state radiatively driven outflows. In addition to the silicate peak position, we also use synthetic colours calculated from LRS data to study detailed properties of mid-infrared emission. Earlier findings that Miras and SRb/Lb variables exhibit significantly different IR emission properties are confirmed at statistically significant levels in Section 2. We attempt to explain these discrepancies by an interrupted mass-loss model, and provide detailed model testing in Section 3. In Section 4 we discuss the implications.

2 OBSERVED DIFFERENCES IN DUST EMISSION BETWEEN MIRA AND SR STARS

2.1 Distribution of AGB stars in K–12 versus 12–25 colour–colour diagrams

Fig. 1 shows the K–[12] versus [12]–[25] colour–colour diagram taken from IK98[2] (the K data were obtained by Franz Kerschbaum and collaborators). The thick curved short-dashed and long-dashed lines represent tracks for interrupted mass-loss models which are described in detail in Section 3. It is assumed that mass loss abruptly stops and the envelope freely expands thereafter. Because of this expansion the dust temperature at the inner envelope radius decreases. Model tracks for various values ranging from 1200 to 600 K for carbon grains (short-broken lines) and from 700 to 300 K for silicate grains (long-broken lines) are shown in the figure. These tracks demonstrate that the distribution of stars with silicate dust in K–[12] versus [12]–[25] colour–colour diagram can be reproduced by varying T_1 in the range 300–700 K, without any change in the adopted absorption efficiency for silicate grains. The distribution of Mira and non-Mira stars with carbon dust is fairly well described by models with $T_1 = 1200$ K, and thus the assumption of significantly lower T_1 is not required by the data. However, note that such models are not ruled out by the data since all carbon dust models produce similar tracks.

[2] Note that colour definitions are different than in IK98, here we define all colours as $[2]–[1] = -2.5\log(F_2/F_1)$, where F_1 and F_2 are fluxes in Jy.

2.2 *IRAS* LRS differences between oxygen-rich mira and SR stars

The oxygen-rich stars usually show infrared spectra indicating silicate dust. Owing to many features in their LRS spectra, such stars are especially well suited for a comparative study of various subclasses. For this reason, in the rest of this work we limit our analysis to oxygen-rich stars. The stars without *IRAS* LRS data are excluded and the final list includes 342 sources, consisting of 96 Mira stars, 48 SRa, 140 SRb and 58 Lb stars. According to Jura & Kleinmann (1992) and Kerschbaum & Hron (1992), the evolutionary state of the SR variables can be determined from their pulsation period, P: stars with $P < 100$ d should be in the early-AGB phase, while stars with $P > 100$ d are in the TP-AGB phase. It has been suggested that only stars in the TP-AGB phase suffer significant mass loss (e.g. Vassiliadis & Wood 1993). We have cross-correlated this list with the General Catalogue of Variable Stars (GCVS, Kholopov et al. 1988) and extracted the pulsational period for SR stars, when available. We find 57 stars with $P < 100$ d and 130 with $P \gtrsim 100$ d.

We divide the stars from the list into several subsamples and analyse the properties of each group separately:

(i) Mira stars;
(ii) non-Mira stars, including SRa, SRb and Lb types, hereafter NM;
(iii) SRa stars, in order to test the possibility that SRa are a spurious class containing a mixture of Mira and SRb variables;
(iv) short-period ($P < 100$ d) SR stars, hereafter spSR;
(v) long-period ($P > 100$ d) SR stars, hereafter lpSR.

Owing to the heterogeneous nature of the samples from which the KHc list is derived, and to the limitations of the *IRAS* catalogue (e.g. source confusion in the galactic plane), our sample is not statistically complete and may have hidden biases. However, it is

Downloaded from https://academic.oup.com/mnras/article/324/4/1117/1316774 by guest on 21 August 2022

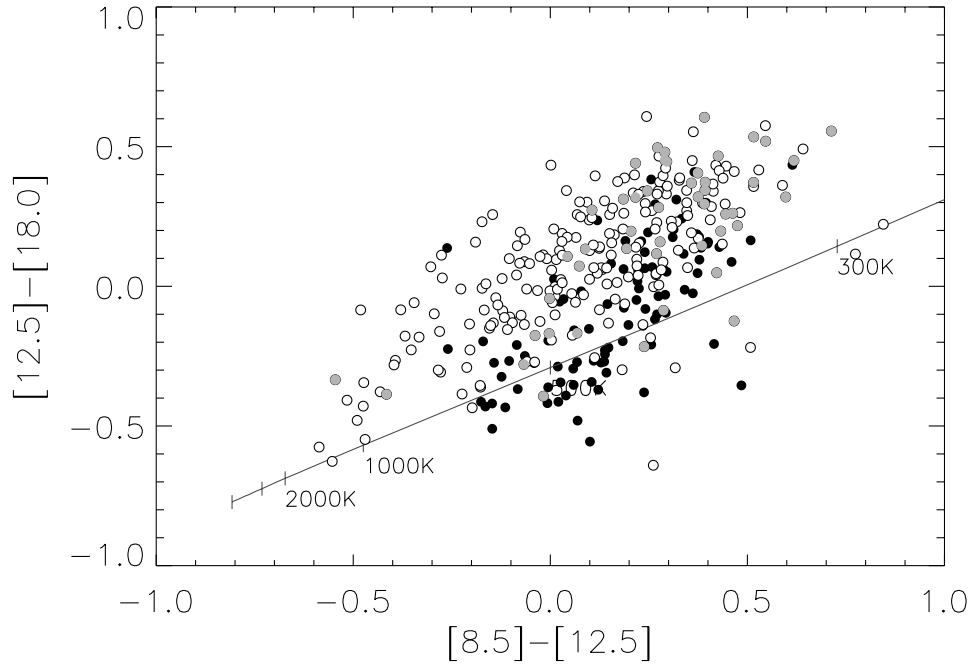

Figure 2. The [12.5]–[18.0] versus [8.5]–[12.5] colour–colour diagram based on synthetic fluxes obtained from LRS data (see Section 2.2.1). Mira stars are shown as full circles, NM stars as open circles, and SRa stars as grey dots. The line is the locus of blackbody colours parametrized by the temperature, as marked. Note the different distribution of Mira and NM stars.

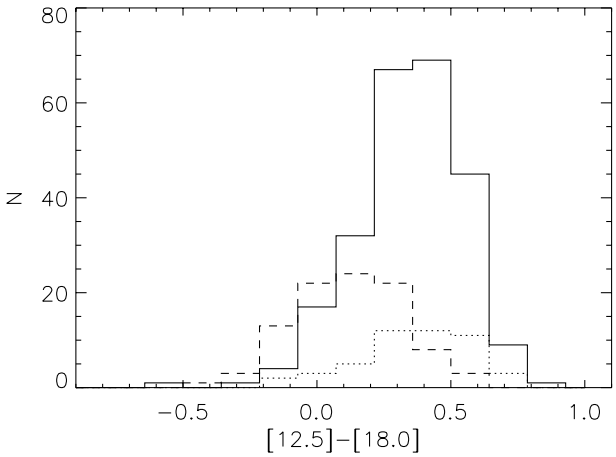

Figure 3. Distribution of the [12.5]–[18.0] colour excess, relative to a blackbody with the same [8.5]–[12.5] colour temperature, for Mira (broken line), NM (full line) and SRa (dotted line) stars. Non-Mira stars have ~ 0.2 mag larger colour excess than Mira stars (see Table 1).

Table 1. Sample statistics (a) and significance of statistical tests (b) for the [12.5]–[18.0] colour excess. Samples have different σ at the 99 per cent confidence level if the variance F-test returns a significance of 0.01 or smaller, and different mean values if student's t-test returns a significance of 0.01 or smaller.

(a) Sample	Median	Mean	σ	N
Mira	0.10	0.11	0.18	96
NM	0.34	0.32	0.18	246
SRa	0.37	0.33	0.19	48
spSR ($P < 100$ d)	0.37	0.36	0.17	57
lpSR ($P \gtrsim 100$ d)	0.32	0.30	0.20	130

(b) Sample	F-test	t-test	result
Mira versus NM	0.90	6×10^{-20}	Same σ, diff. mean
SRa versus Mira	0.70	2×10^{-10}	Same σ, diff. mean
SRa versus NM	0.60	0.71	Same σ and mean
spSR versus lpSR	0.16	0.05	Same σ and mean

sufficiently large to allow a critical study of the correlation between variability type and properties of infrared emission for oxygen-rich galactic AGB stars.

2.2.1 Mid-IR colours

The LRS spectra for a large number of sources can be compared efficiently by using synthetic colours based on 'fluxes' obtained by convolving LRS spectra with suitably defined narrow filters. We utilize the photometric system developed by Marengo et al. (1999; hereafter M99) as a diagnostic tool for mid-IR imaging of AGB stars. The system is designed to be sensitive to the strength of the 9.7-μm silicate feature and to the slope of the dust continuum emission in the 7–23μm spectral range. We calculate synthetic fluxes from LRS data by using 10 per cent passband filters with Gaussian profiles centred at 8.5, 12.5, and 18.0 μm. The resulting [8.5]–[12.5] versus [12.5]–[18.0] colour–colour diagram for all stars in the sample is shown in Fig. 2. Mira stars are shown as full circles, NM stars as open circles and SRa stars as grey dots. The line shows the locus of blackbody colours parametrized by the temperature, as marked in the figure.

The differences between Mira and NM sources are evident. Mira stars are grouped around the blackbody track, with $-0.1 \lesssim$ [8.5]–[12.5] $\lesssim 0.4$. This region, as shown by M99, is well described by envelopes with hot dust and intermediate optical depth $1 \lesssim \tau_V \lesssim 30$. All NM stars have instead a much larger spread in the [8.5]–[12.5] colour, and a redder [12.5]–[18.0] colour. The SRa stars have a distribution similar to other NM stars, except that their [8.5]–[12.5] colour is on average redder than for the whole sample, and in the range observed for Mira stars.

Downloaded from https://academic.oup.com/mnras/article/324/4/1117/1316774 by guest on 21 August 2022

We provide a quantitative test of the Mira/NM separation in the [12.5]−[18.0] versus [8.5]−[12.5] colour−colour diagram in Fig. 3, and summarize it in Table 1. The histogram in Fig. 3 shows the distributions of the [12.5]−[18.0] colour excess, defined as the difference between [12.5]−[18.0] colour and the colour of a blackbody with the same [8.5]−[12.5] colour temperature,[3] for Mira, SRa and NM stars. The mean value of this excess is ∼0.11 for Miras, ∼0.32 for NM and ∼0.33 for SRa. The 0.2-mag difference between the mean values of Mira and NM distributions is slightly larger than the dispersion of the two samples, as measured by the sample variance ($\sigma \sim 0.18$ for both Miras and NM). We tested this result with a student's *t*-test for the mean values, finding that the difference between the two populations is statistically significant (see Table 1 for details). We also performed the same analysis for the spSR and lpSR subsamples and found that they have a similar mean colour excess (0.36 and 0.30 mag); the difference of 0.06 mag is not significant.

These two statistical tests suggest that, regarding their mid-IR [8.5]−[12.5] and [12.5]−[18.0] colours, Mira stars and NM stars are different. That is, given the envelope optical depth, as measured by the [8.5]−[12.5] colour, NM stars show more cold emission measured by the [12.5]−[18.0] colour. Among the SR sources, the mid-IR colours do not correlate with the pulsational period. Assuming the validity of the correlation of Kerschbaum & Hron (1992) between the pulsational period and AGB evolution, this suggests that SR stars form similar circumstellar envelopes in the early and thermally pulsing AGB phases. The similarity of SRa with NM in general indicates that the SRa sample is not significantly contaminated by Mira stars.

2.2.2 *The peak wavelength of the '9.7-μm' silicate feature*

Following KHc, we also determine the peak wavelength of the '9.7-μm' silicate feature for all sources in the sample. Such studies were done first by Little-Marenin & Little (1990) who tried to classify LRS spectra for a large sample of AGB stars. They found that their subsample of SR and L variables showed a narrower silicate feature, and shifted to the red compared with Mira stars. A similar analysis was performed by Hron et al. (1997) for a larger number of sources, accounting for the dust continuum emission by fitting it with a separate blackbody. They confirmed the differences between the two classes, finding a shift of about 0.3 μm in the silicate feature peak position.

We determine the silicate feature peak position by fitting a fifth-degree polynomial to each LRS spectrum in the 9–11μm wavelength range. This fitting procedure removes the effect of noise and eventual secondary features, producing 'smooth' spectra where the position of the maximum can be easily recognized. The wavelength of the maximum of the fitting polynomial in the given interval is then assumed to be the position of the 'true' silicate peak. With this technique we measured the position of the silicate peak for 85 Miras and 162 NM; for the remaining sources (11 Miras and 84 NM) the fitting procedure failed either because of the excessive noise in the spectra, or owing to the absence of a significant feature. Many of the sources for which the silicate feature is too weak to measure the position of its peak are Lb stars of LRS Class 1n.

The results for the position of the silicate feature peak are listed in Table 2 and shown as histograms in Fig. 4. The mean values for Miras and NM are $\langle\lambda_{\rm max}\rangle_{\rm Mira} \simeq 9.86\mu$m and $\langle\lambda_{\rm max}\rangle_{\rm NM} \simeq 10.01\,\mu$m, respectively; the medians are 9.87 and 10.08 μm. Note the different standard deviation σ_λ of the two samples, almost twice as large for NM (∼0.42 μm) than for Miras (∼0.28 μm); this difference is 99.9 per cent statistically significant according to the *F*-test. The student's *t*-test for the mean values, performed between the two samples (with unequal variances), confirms the separation of the Mira and NM populations with respect to their $\lambda_{\rm max}$ at a high (99.95 per cent) significance level, in agreement with the results of Hron et al. (1997).

We performed the same test on the SRa class alone, finding $\langle\lambda_{\rm max}\rangle_{\rm SRa} \simeq 10.08\mu$m, and $\sigma_\lambda \simeq 0.41$, consistent with the results for the whole NM class. This further indicates that the SRa subsample does not contain a significant number of misclassified Miras. The $\langle\lambda_{\rm max}\rangle$ values for the NM subsets with $P \gtrsim 100$ d and $P < 100$ d are 10.07 and 10.09 μm, respectively, and the σ_λ are 0.43 and 0.39 μm. The difference in the σ_λ of the two subsamples is not significant, confirming that the two subsets are part of the same population, in agreement with the analysis of synthetic mid-IR colours.

Table 2. Sample statistics (a) and significance of statistical tests (b) for the peak Position of the silicate 9.7-μm feature. Samples have different σ at the 99 per cent confidence level if the variance *F*-test returns a significance of 0.01 or smaller, and different mean values if student's *t*-test returns a significance of 0.01 or smaller.

(a)

Sample	Median	Mean	σ	*N*
Mira	9.87	9.86	0.28	85
NM	10.07	10.01	0.42	162
SRa	10.10	10.08	0.41	37
spSR ($P<100$ d)	10.09	10.04	0.43	31
lpSR ($P\gtrsim100$ d)	10.07	10.02	0.38	95

(b)

Sample	*F*-test	*t*-test	Result
Mira versus NM	5×10^{-5}	5×10^{-4}	Diff. σ and mean[b]
SRa versus Mira	6×10^{-3}	4×10^{-3}	Diff. σ and mean[b]
SRa versus NM	0.82	0.43	Same σ and mean
spSR versus lpSR	0.41	0.87	Same σ and mean

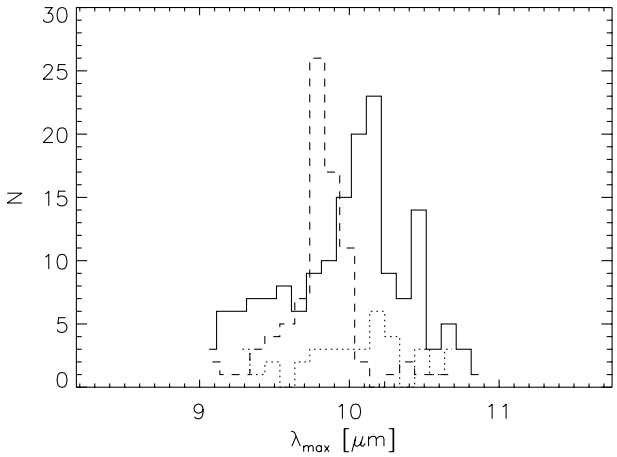

Figure 4. Distribution of the peak position of the silicate '9.7-μm' feature for Mira (broken line), NM (full line) and SRa (dotted line) stars. The NM stars have the feature shifted for ∼0.2 μm with respect to the Miras.

[3] Note that the blackbody assumption is not crucial since it simply provides a reference point.

Downloaded from https://academic.oup.com/mnras/article/324/4/1117/1316774 by guest on 21 August 2022

2.3 Interpretation of the observed differences

We have shown that oxygen-rich Mira and non-Mira stars have statistically different properties of their infrared emission. In particular, we find

(i) a different distribution in the K−[12] versus [12]−[25] colour−colour diagram;
(ii) different [12.5]−[18.0] excess emission;
(iii) different peak−position of the silicate feature.

As shown by IK98 (cf. Fig. 1), these differences are not in agreement with the 'standard' steady-state radiatively driven wind models: while they can reproduce the properties of the Mira sample, they cannot explain the infrared emission from non-Mira stars. There are three ways to augment the 'standard' models without abandoning the hypothesis of a radiatively driven outflow: changing the input (stellar) spectrum, altering the spectral shape of dust opacity and employing a different dust density distribution.

The star in the 'standard' models is assumed to radiate as a 2500 K blackbody. The observed differences in the K−[12] versus [12]−[25] colour−colour diagram could imply that the typical stellar temperature is significantly different for Mira versus non-Mira stars, or that the blackbody spectral shape is not an adequate description of the true stellar spectrum [e.g. owing to an absorption feature in the *K*-band such as the H_2O feature seen in IRTS data by Matsuura et al. (1999)]. A different input spectrum would affect the model K flux, and to some extent the 12-μm flux in optically thin envelopes. However, such a change cannot account for the observed differences in the mid-infrared region (items (ii) and (iii) above) where the flux is dominated by dust emission.

It is possible to produce model spectra in agreement with data for non-Miras by altering the adopted spectral shape of absorption efficiency for silicate grains. There are two required changes. First, the ratio of silicate feature strengths at 18 and 10 μm has to be increased for a factor of about 2–3.[4] Such a change results in a model track in the K−[12] versus [12]−[25] diagram which leaves the Rayleigh−Jeans point at a larger angle (with respect to the K−[12] axis) than before, and passes through the observed source distribution. These models also produce larger [12.5]−[18.0] excess emission in agreement with item (ii) above. In order to account for item (iii) above, a second change is required: the peak position of the '9.7-μm' feature has to be shifted longwards for about 0.2–0.3 μm. For example, the inclusion of Al oxides can shift the peak position to longer wavelengths (Speck et al. 2000). We conclude that, although the postulated changes might seem ad hoc and have little support from model dust optical properties, the possibility of non-Miras having somewhat different grains cannot be ruled out by using near-IR and *IRAS* data alone.[5]

The third way to alter the model spectra predicted by 'standard' models is to decrease T_1, the dust temperature at the inner envelope edge, which is usually assumed to correspond to the dust condensation temperature (∼1000 K). The removal of hot dust reduces the flux at 12 μm significantly more than the fluxes in *K*-band and at 25 μm, and produces model tracks in agreement with the source distribution in the K−[12] versus [12]−[25] colour−colour diagrams (cf. Fig. 1), and larger [12.5]−[18.0] excess emission. It is remarkable that the models with a low T_1 are also capable of explaining the differences between the peak position of the silicate feature. The top panel in Fig. 5 displays two model spectra obtained with visual optical depth of 0.6, and T_1 = 300 K (broken line) and 700 K (full line). The dotted line shows the stellar spectrum. Because the hot dust has been removed in the model with T_1 = 300 K, both the blue and red edges of the 10-μm silicate emission feature are shifted longwards by about 0.2–0.3 μm. While the peak position in the model spectra is exactly the same in both models, the addition of noise to the models would make the whole feature for T_1 = 300 K model appear shifted longwards. Thus, assuming a lower T_1 in models for NM stars can account for all three items listed above. Such models are described further in the next section.

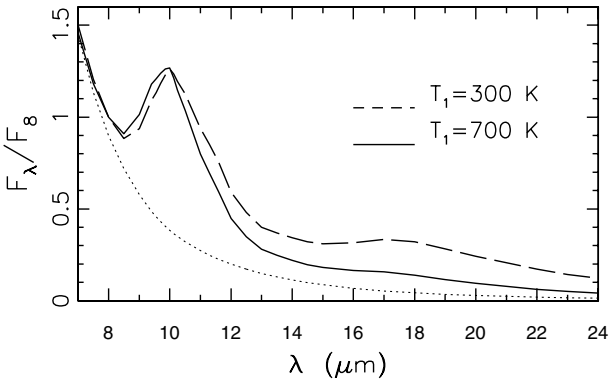

Figure 5. Model spectra in the LRS region obtained for silicate grains with the visual optical depth of 0.6 and 2 values of the dust temperatures at the inner envelope radius, T_1 (full and broken curves). Dotted curve shows the stellar contribution to the spectra. Note that the silicate '9.7'-μm feature appears weaker and is shifted longwards for T_1 = 300 K, relative to the position obtained for T_1 = 700 K, although both are calculated with the same grain optical properties.

We conclude that the two most probable explanations for the observed differences in infrared emission between Mira and non-Mira stars are either different grain optical properties, or the lack of hot dust in non-Mira stars. The possibility that employing different types of grains could reproduce the observed differences between Mira and NM stars requires an extensive modelling effort and will be analysed in a separate publication (Helvaçi et al., in preparation). Here we discuss low-T_1 models and show that they are consistent with the infrared emission observed for NM stars. Various observational techniques for distinguishing these two hypothesis are further discussed in Section 4.

3 MODELS

3.1 Model assumptions and predictions

We calculate model spectra by using the DUSTY code (Ivezić, Nenkova & Elitzur 1997). It is assumed that the star radiates as a 2500 K blackbody. Silicate warm dust opacity is taken from Ossenkopf, Henning & Mathis (1992), with the standard MRN grain size distribution (Mathis, Rumpl & Nordsiek 1977). The dust density is described by r^{-2} with an arbitrary inner envelope radius, r_1. The outer envelope radius is irrelevant as long as it is much larger than r_1, and we fix it at the value of 3×10^{17} cm. In the interrupted mass-loss model, the inner envelope radius increases with *t*, the time elapsed since the mass loss stopped as

$$r_1 = r_1(0) + vt = r_1(0) + 3.2 \times 10^{13}\,\mathrm{cm}\, v_{10} t_{\mathrm{yr}} \quad (1)$$

[4] This strength ratio is not a very constrained dust property, but the uncertainty seems to be smaller than a factor of 2 (Draine & Lee 1984).
[5] Indeed, Sloan, Levan & Little-Marenin (1996) found that the '13-μm' feature occurs somewhat more frequently in SRb stars (75–90 per cent) than in all AGB stars with silicate dust (40–50 per cent).

Downloaded from https://academic.oup.com/mnras/article/324/4/1117/1316774 by guest on 21 August 2022

where $t = t_{\rm yr}$ yr, the expansion velocity $v = v_{10} 10\,{\rm km\,s^{-1}}$ and $r_1(0)$ is the envelope inner radius at $t = 0$. This radius depends on the grain optical properties and dust condensation temperature, and the stellar temperature and luminosity (IE97). For typical values

$$r_1(0) = 3 \times 10^{14}\,{\rm cm}\,L_4^{1/2}, \tag{2}$$

where the stellar luminosity $L = L_4 10^4\,{\rm L}_\odot$.

We specify r_1 by the temperature at the inner edge at time t, T_1. This temperature decreases with time because the distance between the star and the envelope inner edge increases. This relationship is approximately given by (IE97, equation 30)

$$\frac{T_1}{T_1(0)} = \left(\frac{r_1(0)}{r_1}\right)^{2/(4+\beta)} \tag{3}$$

where β is the power-law index describing the opacity wavelength dependence. This expression is strictly correct only in the optically thin regime, and furthermore, the silicate dust opacity cannot be described by a simple power law. However, it provides a good description of detailed model results with $\alpha = 2/(4+\beta) \sim 0.40 \pm 0.05$. Combining the above expressions gives

$$\frac{T_1}{T_1(0)} = \left(1 + 0.1\frac{v_{10} t_{\rm yr}}{L_4^{1/2}}\right)^{-\alpha}. \tag{4}$$

As already indicated in Section 2 (cf. Fig. 1), the distribution of SR stars in the K–[12] versus [12]–[25] colour–colour diagram implies a lower limit on T_1 of $\sim$300 K. Assuming $T_1(0) = 800$ K, $v_{10} = L_4 = 1$ implies a time-scale of 100 yr.

The second free parameter is the dust optical depth which we specify as the visual optical depth, τ_V. This parameter controls the amount of dust and increases with $\dot{M}$, the mass-loss rate during the high-mass-loss phase. The steady-state[6] radiatively driven wind models give for silicate dust (Elitzur & Ivezić 2001)

$$\dot{M} = 2 \times 10^{-6}\,{\rm M}_\odot\,{\rm yr}^{-1}\,\tau_V(0)^{3/4} L_4^{3/4} \left(\frac{r_{\rm gd}}{200}\right)^{1/2} \tag{5}$$

where $r_{\rm gd}$ is the gas-to-dust ratio and τ_V (0) is the optical depth before the mass loss stops. Note that $\dot{M} \propto \tau_V^{3/4}$ rather than $\dot{M} \propto \tau_V$ owing to dust drift effects.

After the mass loss stops, the optical depth decreases with time because it is inversely proportional to r_1 owing to the envelope dilution

$$\frac{\tau_V}{\tau_V(0)} = \left(1 + 0.1\frac{v_{10} t_{\rm yr}}{L_4^{1/2}}\right)^{-1}. \tag{6}$$

The models could be parametrized by $\dot{M}$ and r_1 (or t) instead of τ_V and T_1. However, in such a case the parametrization of a model spectrum would involve at least two additional parameters (L and $r_{\rm gd}$) and would artificially introduce a four-dimensional fitting problem. As the scaling properties of the radiative transfer imply (IE97), the described model is only a two-dimensional problem fully specified by τ_V and T_1. It is only the correspondence between these two parameters and other quantities such as $\dot{M}$ that involves additional assumptions about, for example, $r_{\rm gd}$.

In the interrupted mass-loss model the changes of T_1 and τ_V as the envelope expands are correlated. Combining equations (4) and (6) gives

$$\frac{T_1}{T_1(0)} = \left(\frac{\tau_V}{\tau_V(0)}\right)^{\alpha}, \tag{7}$$

and thus during the expansion

$$T_1 \tau_V^{-\alpha} = C = \text{ constant} \tag{8}$$

where the value of constant C is determined by $\dot{M}$ during the high mass-loss phase. The model predicts that the distribution of best-fitting T_1 and τ_V should resemble a strip in the τ_V–T_1 plane the width of which is determined by the intrinsic distribution of the mass-loss rates during the high mass-loss rate phase, and with the position along the strip parametrized by the time since the mass loss stopped.

Another model prediction is for the T_1 distribution of sources in an unbiased sample (or equivalently for the τ_V distribution since τ_V and T_1 are correlated). Equation (4) shows that the first derivative of T_1 decreases with time and thus the number of observed sources should increase as T_1 decreases. Assuming ${\rm d}N(T_1) \propto {\rm d}t(T_1)$, where d$N$ is the number of sources in a given T_1 bin, the model implies

$$\frac{{\rm d}N}{{\rm d}T_1} \propto T_1^{-(1+\alpha)/\alpha} \propto T_1^{-3.5}. \tag{9}$$

This prediction applies for sources with T_1 smaller than the dust condensation temperature, $T_{\rm c}$. The number of sources with T_1 comparable to $T_{\rm c}$ depends on the duration of the high-mass-loss phase such that the ratio of the number of sources with $T_1 < T_{\rm c}$, to the number of sources with $T_1 \sim T_{\rm c}$, is equal to the ratio of times spent in the low- and high-mass-loss phases.

To summarize, the interrupted mass-loss models assume a sudden drop in the mass-loss rate after which the envelope freely expands. The infrared spectrum emitted during this phase depends on only two free parameters, the temperature at the inner envelope edge, T_1 and the envelope optical depth τ_V. Both of these quantities decrease with time in a correlated way described by equation (8).

Note that the two free parameters imply a two-dimensional family of model LRS spectra. It is usually assumed that the shape of an LRS spectrum for silicate grains is fully specified by the 9.7-μm silicate feature strength. However, in this model even for a fixed 9.7-μm silicate feature strength, there is a family of spectra with differing shapes owing to the varying second parameter. We find that the ratio of fluxes at 18 and 10 μm, F_{18}/F_{10}, is a convenient observable, in addition to the 9.7-μm silicate feature strength, which can be used to parametrize the LRS spectra. That is, each combination of T_1 and τ_V corresponds to a unique combination of the 9.7-μm silicate feature strength and the F_{18}/F_{10} ratio, and each such LRS spectrum corresponds to a unique pair of T_1 and τ_V. Of course, assuming that all stars have the same L, $r_{\rm gd}$ and v_{10}, a given LRS spectrum corresponds to a unique combination of $\dot{M}$ and r_1, and vice versa.

This two-dimensionality of LRS spectra is illustrated in Fig. 6 which displays a time evolution of model spectra after the mass-loss interruption (for details see the figure caption). Each spectrum is fully characterized by τ_V and T_1, which equivalently can be expressed as time t, marked in each panel, and mass-loss rate indicated on top of each column. The corresponding values of LRS class, which measures the 9.7-μm silicate feature strength, and the $F_{18}F_{10}$ ratio are also marked in each panel. Note that some spectra have the same LRS class (e.g. $t = 0$ yr in the first column, $t = 25$ yr in the second column, and $t = 50$–75 yr in the third column) and

[6] The steady-state assumption does not strictly apply here. However, the crossing time for the acceleration zone ($\sim 2r_1$, corresponding to ~ 10 yr) is much shorter than the presumed duration of the high mass-loss rate phase, and thus equation (5) can be used to estimate approximate mass-loss rate.

Downloaded from https://academic.oup.com/mnras/article/324/4/1117/1316774 by guest on 21 August 2022

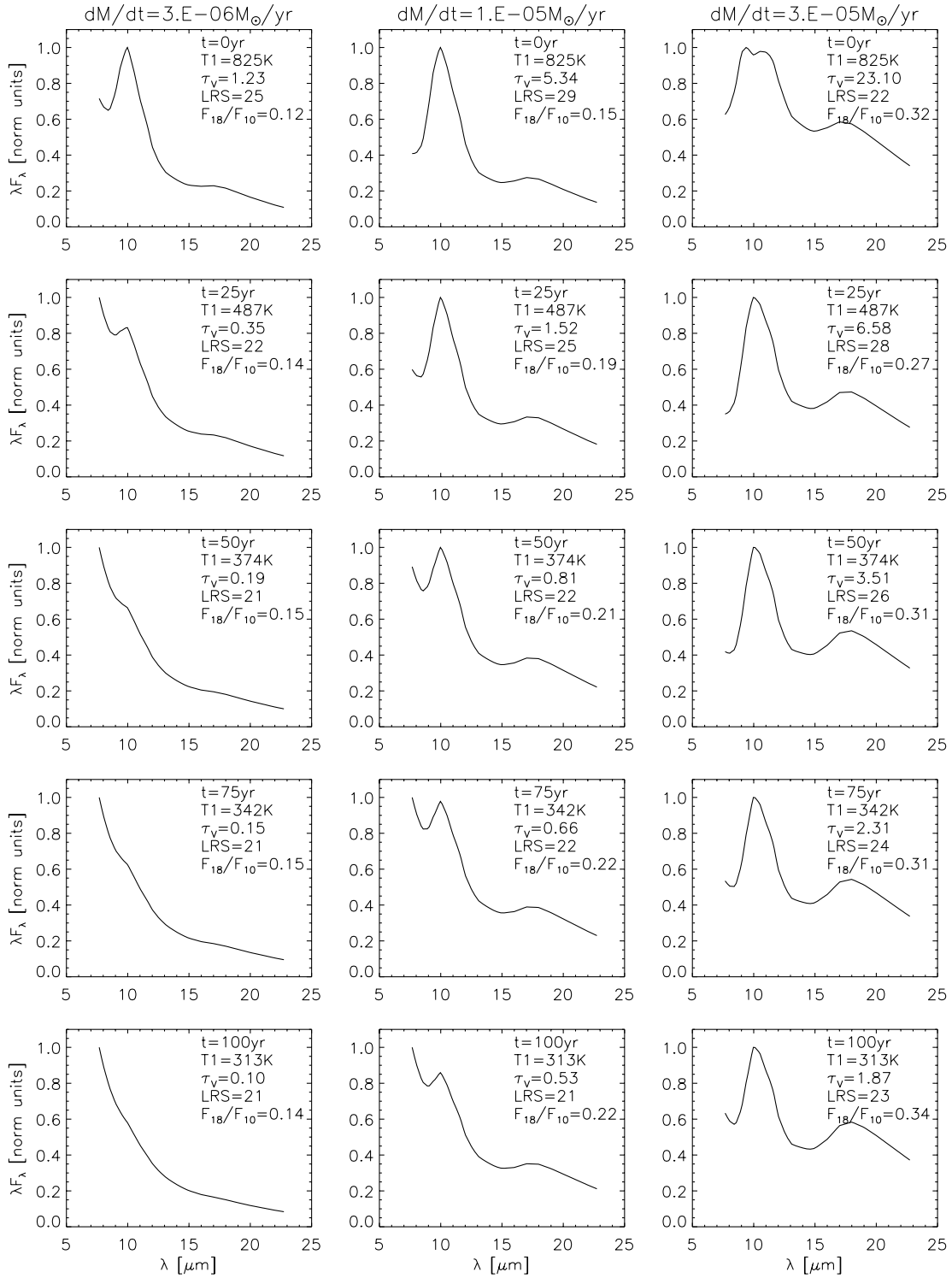

Figure 6. An illustration of the two-dimensionality of LRS spectra. Each column displays a time evolution of model spectra after the mass-loss interruption, calculated in steps of 25 yr. The spectra in three columns are displayed for different mass-loss rates before the interruption, increasing from left to right, and indicated on top of each column. Each spectrum is fully characterized by τ_V and T_1, which equivalently can be expressed as time t, marked in each panel, and mass-loss rate. The corresponding values of LRS class, which measures the 9.7-μm silicate feature strength, and the F_{18}/F_{10} ratio are also marked in each panel (see text for details).

yet are clearly distinguishable both by their overall shape and the values of the F_{18}/F_{10} ratio. Another important detail is that the spectra with comparatively large F_{18}/F_{10} ratio are obtained only for comparatively low T_1, as discussed earlier.

While we assume that the mass loss ceases completely, the data provide only a lower limit on the mass-loss rate ratio in the two phases of high and low mass loss. We have explored a limited set of models where the mass-loss rate drops for a factor of 3, 5, 10 and 100, and found that with the available data we cannot distinguish cases when the mass-loss rate drops by more than a factor of 5.

Downloaded from https://academic.oup.com/mnras/article/324/4/1117/1316774 by guest on 21 August 2022

Thus, this is a lower limit on the ratio of mass-loss rates in the two phases.

We have computed ~2000 model spectra parametrized on logarithmic grids with 62 τ_V steps in the range 10^{-3}–350, and 32 T_1 steps in the range 100–1400 K. Models calculated on a finer grid in either τ_V or T_1 vary less between two adjacent grid points than typical noise in the data. A subset of models with T_1 restricted to the interval 600–1400 K is hereafter called 'hot-dust' models. We fit these models separately to all sources in order to test whether 'cold-dust' models (with $T_1 < 600$ K) are necessary to improve the fits.

3.2 Fitting technique

The best-fitting model for each source is found by using a χ^2-minimization routine applied to the source and model spectra in the *IRAS* LRS spectral region (8–23 μm). The χ^2 variable is defined as

$$\chi^2 = \frac{1}{N-2}\sum_{i=1}^{N}\frac{[\lambda_i F_\lambda^{\rm O}(\lambda_i) - \lambda_i F_\lambda^{\rm M}(\lambda_i)]^2}{\sigma_{\rm O}^2 + \sigma_{\rm M}^2}, \quad (10)$$

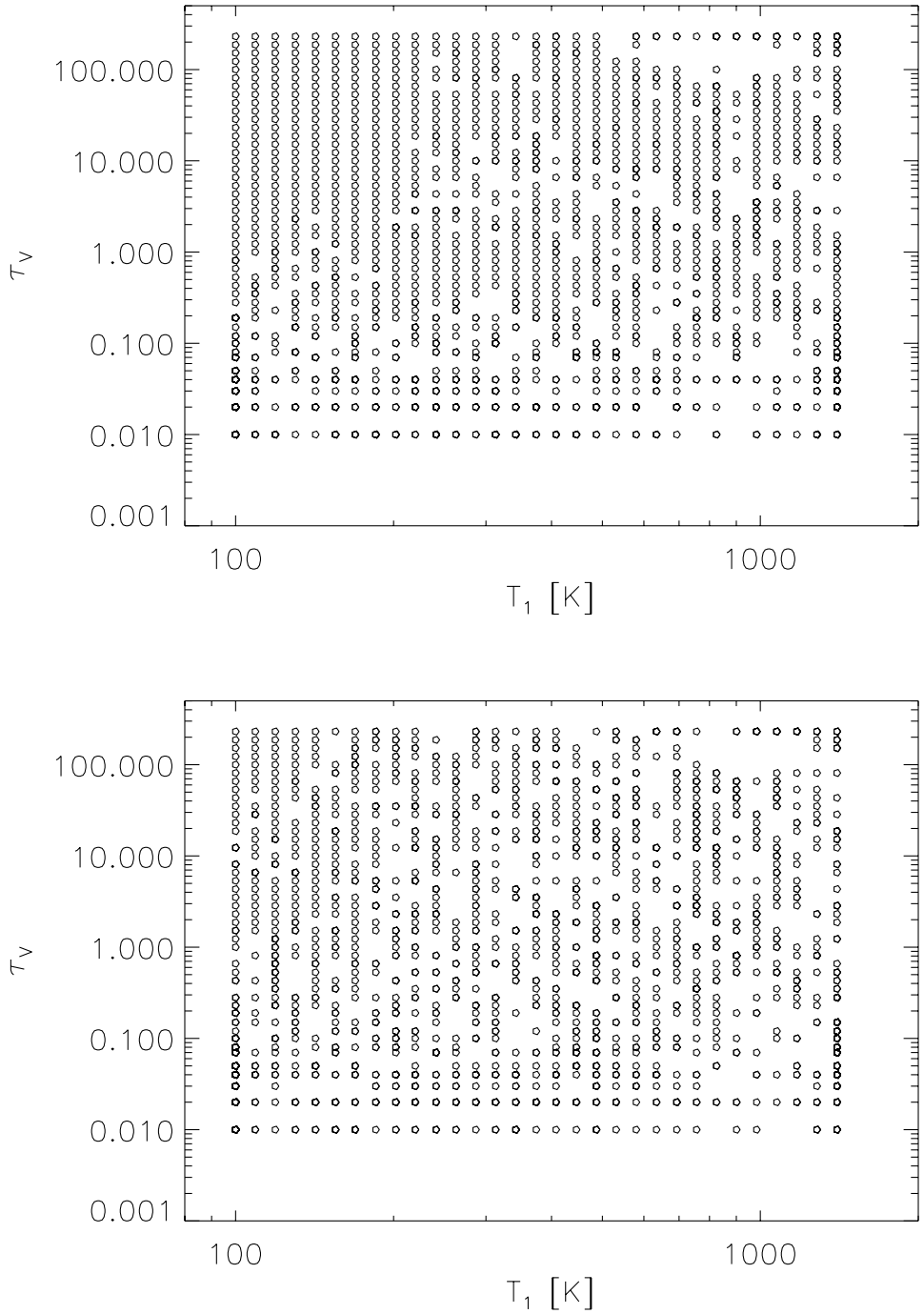

Figure 7. Test diagram of the fitting procedure. Gaussian noise with S/N = 10 (top) and 5 (bottom) is added to the full grid of models and the resulting spectra are fitted with the noiseless spectra. Each circle represent a successful recovery of the true τ_V and T_1, while the missing points are incorrectly identified models. The majority of 'failed' models fall on to a neighbouring grid point.

Downloaded from https://academic.oup.com/mnras/article/324/4/1117/1316774 by guest on 21 August 2022

where $F_\lambda^{\rm O}$ is the observed flux and $F_\lambda^{\rm M}$ is the model flux. The error $\sigma_{\rm O}$ of the *IRAS* LRS data was estimated as the root-mean-square (rms) difference between the raw and a cubic spline smoothed LRS spectra. The model error $\sigma_{\rm M}$ is taken as the rms difference between the two closest models in the parameter space. The χ^2 variable was then normalized to the number of wavelengths N, minus the number of fitting parameters (τ_V and T_1). By comparing each source spectrum with all spectra in a given model set, we determine χ^2 and select a model with the lowest χ^2 as the best-fitting model. This procedure is repeated independently for the set of all models, and for the 'hot-dust' subset.

As discussed in the previous section, the interrupted mass-loss model predicts a particular distribution of sources in the τ_V–T_1 plane, which may be affected by hidden systematic biases in the fitting procedure. In order to assess the level of such biasing, we perform a 'self-fit' test for all models in the sample. We add Gaussian noise similar to the noise in the LRS data to each of the DUSTY model spectra and then pass such spectra through the fitting algorithm. We consider two noise levels (signal-to-noise ratio, S/N), S/N = 10 typical for the whole sample and S/N = 5, representative of the stars with the lowest-quality LRS data.

The results are shown in Fig. 7 where each circle represents a point in the model grid; missing points are models for which the true τ_V and T_1 were not recovered because of noise in the 'data'. The majority of such 'failed' fits fall on to a neighbouring grid point. The figure shows that increasing noise can reduce the effectiveness of our procedure. However, the T_1 distribution of the incorrectly identified models is uniform even in the low S/N case, and thus within the limits of our sample the fitting procedure does not introduce significant biasing in the best-fitting parameters.

3.3 Best-fitting model results

The quality of a fit is described by the best-fitting χ^2 variable. A good fit, in which the details of the source spectra are reproduced by the model (e.g. Fig. 8, panel a), generally has $\chi^2 \lesssim 5$. Fits with $5 \lesssim \chi^2 \lesssim 10$ are still acceptable, even though some secondary features in the source spectrum cannot be fully reproduced by the model. This seems to be mainly caused by the inability of the adopted silicate opacity to describe all observed spectral features (e.g. the 13-μm feature). A larger χ^2 ($\gtrsim$10) indicates more serious discrepancies in the fit, that can range from the convergence errors

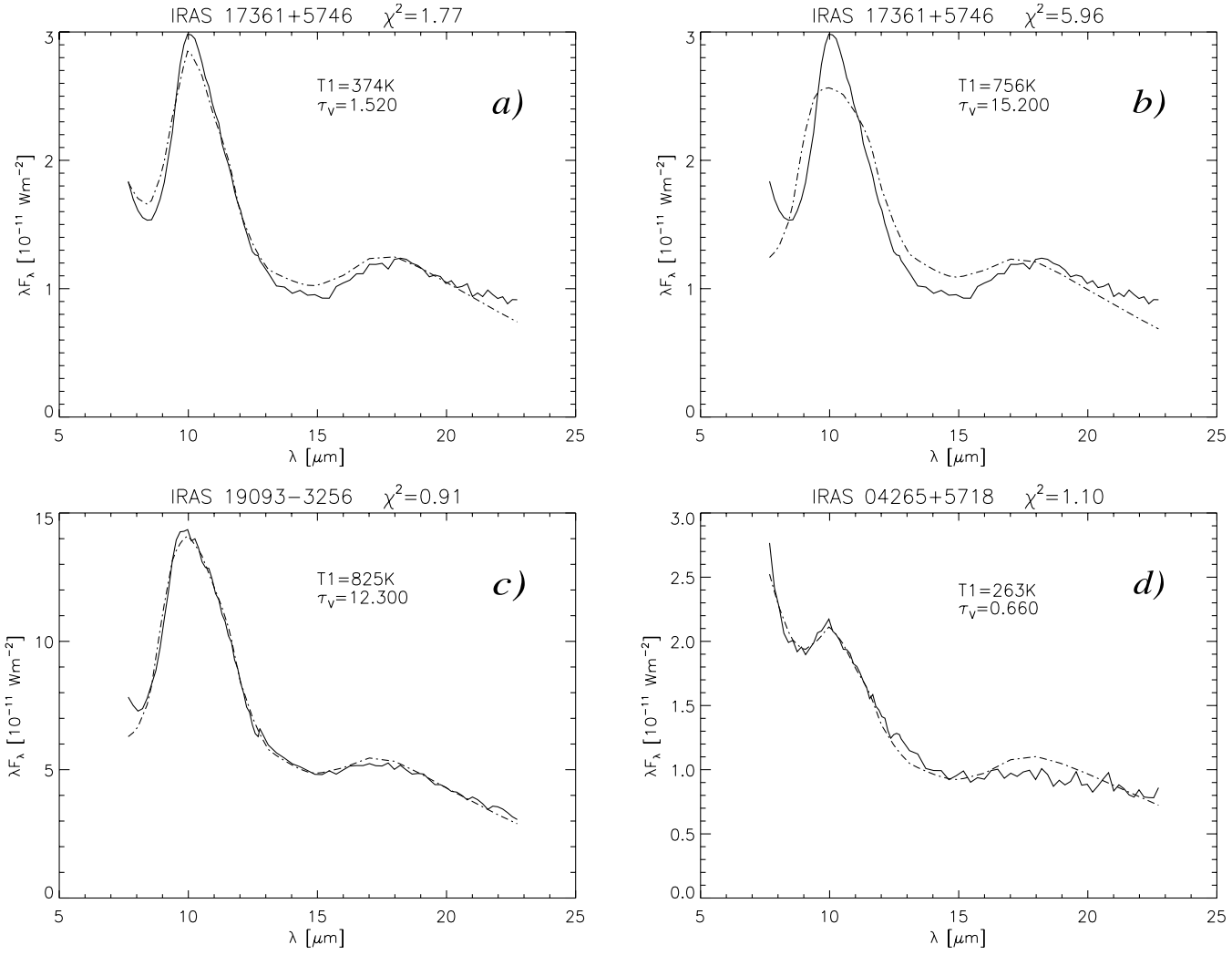

Figure 8. An example of model fits (chain curve) to the *IRAS* LRS data (full curve) for Mira and NM sources. In panel (a) the SRb star TY Dra is fitted with a cold dust model ($T_1 \simeq 370$ K), resulting in a very small χ^2. When the dust temperature is limited to the range 640–1400 K, the fit is unable to reproduce the source spectral energy distribution, as shown in panel (b). The panels (c) and (d) show good quality fits of a Mira star with relatively hot dust ($T_1 = 825$ K) and an SR star with very low inner-shell temperature ($T_1 = 270$ K).

Downloaded from https://academic.oup.com/mnras/article/324/4/1117/1316774 by guest on 21 August 2022

(e.g. when the fitting routine cannot find a well-defined minimum in the χ^2 surface) to poor fits indicating that the adopted opacity and/or radial dust density law are grossly inadequate. Such sources represent less than 10 per cent of the sample.

3.3.1 *The fit quality*

The statistics of the best-fitting χ^2 values for sources with $\chi^2 < 10$ are shown in Table 3. The table reports the fraction of sources in each subsample (Mira, NM, SRa, spSR and lpSR) which cannot be fitted with a χ^2 less than 3 and 10 ('excellent' and 'acceptable' fits). The sources are fitted with two sets of models: 'all-temperatures' models, which include the full T_1 grid and the 'hot dust' models with $T_1 > 600$ K. As is evident, a larger fraction of sources in all subsamples can be fitted within a specified χ^2 limit with the 'all' model set than with the 'hot-dust' models. This is not surprising since the former model set includes a greater variety of spectra owing to the two free parameters, as opposed to the restrictions on one free parameter in the latter set. Nevertheless, the improvement in the best-fit quality is more significant for the NM sample (and all NM subsamples) than for Mira stars. For example, more than a half of NM stars cannot be fitted with a $\chi^2 < 3$ by using 'hot-dust' models, while the inclusion of models with low T_1 decreases their fraction to less than 20 per cent. At the same time, the corresponding fractions for Mira stars are 42 per cent and 35 per cent indicating that low-T_1 models are not necessary to model LRS data of these stars.

An example of the improvement in the fit quality owing to a lower T_1 is shown in Fig. 8. The model spectra are plotted as chain lines and the *IRAS* LRS data as full lines. In panel (a) the SRb star TY Dra is fitted with a cold dust model ($T_1 \simeq 370$ K), resulting in a very small χ^2. When the dust temperature is limited to the range 600–1400 K, the fit is unable to reproduce the source spectral energy distribution, as shown in panel (b). Panels (c) and (d) show good-quality fits of a Mira star with relatively hot dust ($T_1 = 825$ K) and an SR star with very low inner-shell temperature ($T_1 = 270$ K).

Table 3. The best-fitting statistics. The table lists the fraction of sources in each subsample that cannot be fitted with the specified χ^2 criteria. The second and third column correspond to 'all' (temperature) models, and the third and fourth column to 'hot dust' models (see text).

Sample	$\chi^2 \leq 3$ All	$\chi^2 \leq 10$ Models	$\chi^2 \leq 3$ Hot	$\chi^2 \leq 10$ Dust
Mira	35%	3%	42%	12%
NM	18%	1%	54%	22%
SRa	21%	2%	33%	4%
spSR ($P<100$ d)	18%	0%	67%	21%
lpSR ($P\gtrsim100$ d)	21%	2%	48%	6%

3.3.2 *Distribution of best-fitting parameters*

The distribution of best-fitting τ_V and T_1 is shown in Fig. 9. Sources from Mira and NM subsamples are marked by full and open circles, respectively (since the differences in best-fitting parameters between the various subsamples of NM stars are not statistically significant, we consider only Mira/NM subsamples hereafter). A small random offset (up to one-third of the parameter grid step) has been added to each T_1 and τ_V, in order to separate the sources with identical best-fitting parameters, which would otherwise appear as a single point on the diagram. The sources are distributed not randomly but rather along a diagonal strip. The density of sources along the strip has a local minimum for $T_1 \sim 500$ K ($\tau_V \sim 5$), suggesting a division into four regions as shown by the thin full lines. The source counts in the quadrants, labelled clockwise from I to IV, are given in Table 4. Although both Mira and NM stars are present along the whole strip, Mira tend to aggregate in the upper right-hand quadrant with higher T_1 and τ_V. In contrast, NM stars aggregate in the lower left-hand quadrant with $T_1 < 500$ K and $\tau_V < 0.5$.

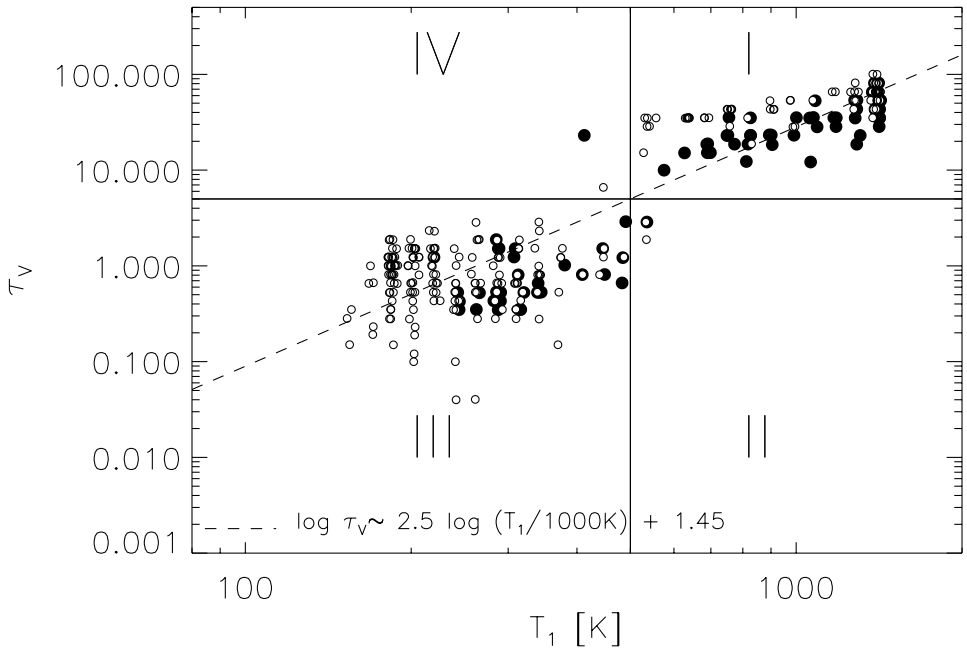

Figure 9. The distribution of best-fitting τ_V and T_1 for Mira stars (full circles) and non-Mira stars (open circles). A small random offset (up to one-third of the parameter grid step) has been added to each T_1 and τ_V, in order to separate the sources with identical best-fitting parameters, which would otherwise appear as a single point on the diagram. The plot is divided in four regions, according to the source segregation; the counts in the four quadrants are given in Table 4.

Downloaded from https://academic.oup.com/mnras/article/324/4/1117/1316774 by guest on 21 August 2022

Table 4. The source distribution in τ_V versus T_1 diagram (see Fig. 9).

Sample	I	II	III	IV
Mira	59	1	32	1
NM	72	2	169	1
SRa	20	1	26	0

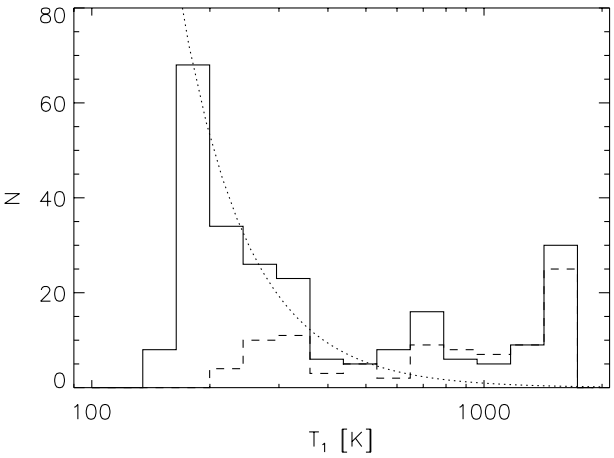

Figure 10. Histogram of best-fitting T_1 for Mira stars (broken line) and NM stars (full line). The broken curve shows relation $dN/d\log(T_1) \propto T_1^{-5/2}$, normalized to the NM bin with $T_1 \approx 200$ K.

The strong correlation between the best-fitting τ_V and T_1 seen in Fig. 9 is probably not because of hidden biasing of the fitting algorithm (cf. Section 3.2). Indeed, such correlation is expected in the interrupted mass-loss model as discussed in Section 3.1. Equation (8) predicts $\tau_V \propto T_1^{1/\alpha} = T_1^{5/2}$ shown as a thick broken line in Fig. 9. The close agreement between the source distribution and predicted correlation is evident. Fitting a power law to the source distribution gives a best-fitting power-law index of 2.8 for Mira stars, and 2.5 for NM stars, consistent with the model prediction, given the uncertainty of α (± 0.05).

Another model prediction pertains to the distribution of best-fitting T_1. For sources in the quiescent phase, equation (9) predicts $dN/dT_1 \propto T_1^{-3.5}$, or equivalently, $dN/d\log(T_1) \propto T_1^{-5/2}$. The histogram of best-fitting T_1 is shown in Fig. 10 for Mira stars (broken line) and NM stars (full line). The relation $dN/d\log(T_1) \propto T_1^{-5/2}$ is shown as a dotted line, normalized to the NM bin with $T_1 \approx 200$ K. It is evident that the T_1 distribution is very different for Mira and NM stars. While this distribution is flat for Mira stars, with about two-thirds of stars having $T_1 > 500$ K, two-thirds of NM stars have $T_1 < 500$ K. These stars closely follow the model prediction for stars, the envelopes of which are freely expanding after their mass loss has stopped.

The low T_1 of the NM distribution in Fig. 10 abruptly ends at $T_1 \sim 200$ K, although the model grid extends to $T_1 = 100$ K. As discussed in IK98, this sharp end may indicate that the mass loss resumes after the quiescent phase because otherwise envelopes with $100 < T_1 < 200$ K should be detected. Equation (4) implies that the time-scale for the envelope expansion until T_1 reaches such a low temperature is $\sim$100 yr. If the mass loss starts again, in less than 10 yr the new shell would occupy the region where the dust temperature is higher than about 600 K, and thus about 10 per cent of stars could be in this phase. The only difference between such a

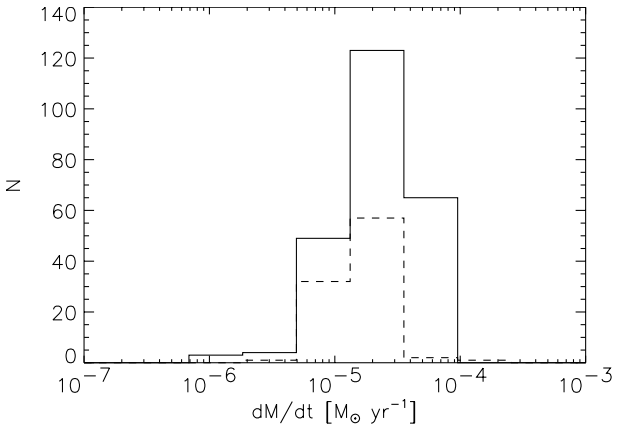

Figure 11. Histogram of derived mass-loss rates for Mira stars (broken line) and NM stars (full line).

double-shell envelope and a steady-state envelope with smooth r^{-2} dust density distribution is the lack of dust with temperatures in the range 200–600 K. Detailed model spectra in the spectral range 5–35μm for such double-shell envelopes show that they are practically indistinguishable from spectra obtained for envelopes with an r^{-2} dust density distribution.

The fraction of NM stars with $T_1 > 500$ K is $\sim\frac{1}{3}$. This fraction provides an upper limit for the duration of high mass-loss phase of $\sim$50 yr. However, it would not be surprising if this estimate is wrong by perhaps a factor of 2 since the analysis presented here only provides a lower limit on the ratio of mass-loss rates in the high- and low-mass-loss phases. Thus, the observations do not strongly exclude the possibility that the duration of both phases may be the same.

3.4 The distribution of mass-loss rates

The width of the strip formed by the source distribution in the τ_V versus T_1 diagram (Fig. 9) is determined by the intrinsic distribution of mass-loss rates. We calculate mass-loss rates from the best-fitting τ_V and T_1 by using

$$\dot{M} = \tau_V^{3/4} \left(\frac{1000\,\mathrm{K}}{T_1}\right)^{5/2} 10^{-6}\,\mathrm{M_\odot\,yr^{-1}} \qquad (11)$$

which is derived by combining equations (5)–(7) and assuming $(T_1(0)/1000\mathrm{K})^{5/2} L_4^{3/4} (r_{\mathrm{gd}}/200)^{1/2} = 0.5$. Fig. 11 shows the histograms of calculated mass-loss rates for Mira stars (broken line) and NM stars (full line). The histograms are rather narrow, and furthermore, they are the same within the uncertainties, according to *F*-test and *t*-test analysis. Such a similarity of mass-loss rates between Mira and NM stars is somewhat surprising because a 'standard' result is that NM stars have several times smaller mass-loss rates than Mira stars (e.g. Habing 1996). A plausible explanation for the smaller mass-loss rates usually derived for NM stars may be the lack of correction for lower T_1 (cf. equation 11) when converting the envelope optical depth to a mass-loss rate. The results presented here indicate that the majority of both Mira and NM stars have mass-loss rates of the order 10^{-5}. An alternative explanation is that the KHc sample of NM stars is biased towards high mass-loss rates, although such an effect is not expected for their selection procedure. Additional selection criteria employed in this work did not affect a sufficiently large number of NM sources to result in such biasing. It is not possible to distinguish between

Downloaded from https://academic.oup.com/mnras/article/324/4/1117/1316774 by guest on 21 August 2022

those two possibilities without a large and unbiased sample with uniformly measured mass-loss rates by an IR-independent method (e.g. molecular emission).

4 DISCUSSION

The analysis presented here shows that the observed differences in infrared emission from oxygen-rich AGB stars of different variability type are statistically significant. Mira stars and NM stars clearly segregate in the K−[12] versus [12]−[25] colour–colour diagram, and also have different detailed properties of their *IRAS* LRS spectra. We find no statistically significant differences between various subsamples of NM stars. The differences between Mira and NM stars are hard to interpret in the context of steady-state wind models. In particular, these models do not provide a satisfactory description of the infrared emission from the majority of NM stars. Possible ways to augment these models include changing the shape of stellar spectrum, employing grains with altered absorption efficiency, or assuming that the majority of NM stars have envelopes without hot dust ($\gtrsim$500 K).

We find that the absence of a hot dust for NMs is the most plausible way to explain the observations, although the available data cannot rule out the possibility that the differences in circumstellar dust chemistry produce the observed differences in infrared emission. For example, Sloan et al. (1996) found that the '13-μm' feature occurs somewhat more frequently in SRb stars (75–90 per cent) than in all AGB stars with silicate dust (40–50 per cent). On the other hand, this difference could be simply caused by different densities in the dust formation region, as pointed out by Speck et al. (2000). We are in the midst of a detailed study exploring the model spectra obtained for a large sample of different dust types and grain size distributions (Helvaçi et al., in preparation).

We provide detailed analysis of models where the absence of hot dust for NM stars is interpreted as an interruption of the mass loss with time-scales of the order of 100 yr, and a drop in the mass-loss rate of at least a factor of 5. In such a case, the envelope freely expands and the dust temperature decreases with time. This hypothesis predicts a correlation $\tau_V \propto T_1^{5/2}$ between the envelope optical depth, τ_V and the dust temperature at the inner envelope edge, T_1, which we find to be consistent with the data. We find that the model prediction for the distribution of best-fitting T_1 also agrees with the data, although this constraint may be plagued by hidden biases in the sample. We interpret the sharp low-T_1 end of the source distribution as evidence that the mass loss resumes and estimate the duration of high-mass-loss phase to be of the same order as the duration of the low-mass-loss phase.

The number of Mira stars with low T_1 is about one-third and it is not clear from the present analysis whether this represents evidence for the interrupted mass loss. It was proposed by Kerschbaum et al. (1996), based on similar number densities and scaleheights, that AGB stars oscillate between NM and Mira phases. This idea was further advanced by IK98 based on their analysis of the source distribution in the K−[12] versus [12]−[25] diagram. However, recent results by Lebtzer & Hron (1999), who compare the abundance of ^{99}Tc in a large sample of SR stars and Mira stars, seem to rule out this hypothesis. The ^{99}Tc abundance is characterized by a quick increase during the first thermal pulse, after which it presumably stays constant (Busso et al. 1992). Consequently, a similar fraction of Tc-rich stars should be found in the Mira and SR samples, contrary to the observations by Lebtzer & Hron who find that a fraction of stars with detectable Tc is lower for SR stars (15 per cent) than for Mira stars (75 per cent).

While the available observations are consistent with the interrupted mass-loss model, the possibility that the observed differences between Mira and NM stars arise from different dust optical properties cannot be excluded by considering photometric data alone. The most obvious and direct test of the interrupted mass-loss hypothesis is mid-IR imaging. When T_1 decreases by a factor of 2, the inner envelope radius increases by about a factor of 4. Such a difference should be easily discernible for a few dozen candidate stars with largest angular sizes, which are already within the reach of the Keck telescopes (e.g. Monnier et al. 1998). Molecular line observations can also be used to infer the gas radial density distribution because various lines form at different radii. For example, the SiO8-7 (347.3-GHz) line is expected to form much closer to the star than, say, the CO3-2 (345.8-GHz) line. If SRb/Lb stars really lack material in the inner envelope, they should have lower SiO8-7/CO3-2 intensity ratios than Miras, provided that the excitation mechanisms are similar. Another, indirect, test can be made by employing mass-loss rates determined in molecular, either thermal or maser observations. For a given mass-loss rate, NM stars should have bluer 12-K colour because their dust optical depth becomes smaller as the envelope expands. While this effect is not very pronounced (difference is about 0.2–0.3 mag), a sufficiently large sample might provide statistically meaningful results.

For a few stars there are available spatially resolved observations (cf. Section 1) and they seem to indicate mass loss changes with short time-scales (<several 100 yr). If proven correct, the mass-loss variations on time-scale of about 100 yr would significantly change our understanding of the stellar evolution on the AGB since the known time-scales are either much shorter (stellar pulsations, ~1 yr), or much longer (He flashes, $\sim 10^5$ yr). However, the time-dependent wind models (Winters 1998) seem to produce mass-loss rate variations with time-scales much longer that the pulsation period which drives the mass loss (~1 yr). These longer time-scales are not fully understood (see, however, Deguchi 1997) and seem to result from the complex interplay between the pulsation and dust formation and destruction mechanisms. While the theoretically obtained time-scales (5–10 years) are shorter than those implied by the observations, the recent developments show that it may be possible to increase the model time-scale to ~100 yr (Winters J.M., private communication). It is not clear why Mira and non-Mira stars would exhibit different behaviours, unless the coupling mechanisms are very sensitive to the details of the pulsation mechanism (see, e.g., Mattei et al. 1997).

Another possibility is that the 100-yr mass-loss rate modulations are caused by the luminosity variations on similar time-scales (Sahai et al. 1999). Recent work based on the analysis of stars observed by both the *IRAS* and *Hipparcos* surveys (Knauer, Ivezić & Knapp 2001) shows that the extensive mass loss on the AGB seems to require a threshold luminosity of $\sim 2000\,L_\odot$. If the luminosity of non-Mira stars oscillates around this value, then the resulting mass-loss rate would be in agreement with the model assumptions discussed here. Within this hypothesis Mira stars could have slightly larger luminosities (for perhaps a factor of 2) and exhibit a steady mass loss, a possibility that seems to be consistent with the *P–L* relation since Mira stars have somewhat longer periods that SR stars (Whitelock 1986).

ACKNOWLEDGMENTS

We are grateful to Franz Kerschbaum for providing to us with *JHKLM* data without which this work would have not been

Downloaded from https://academic.oup.com/mnras/article/324/4/1117/1316774 by guest on 21 August 2022

possible. We thank Martin Jan Winters, Mikako Matsuura, Mathias Steffen, Janet Mattei, John Monnier, Joseph Hron, Moshe Elitzur, Maia Nenkova, Dejan Vinković and Mustafa Helvaçi for illuminating discussions. We also thank the referee, Angela Speck, for comments which helped us improve the presentation. This work was partially supported by NSF grant AST96-18503 to Princeton University.

REFERENCES

Bedijn P. J., 1987, A&A, 186, 136
Busso M., Gallino R., Lambert D. L., Raiteri C. M., Smith V. V., 1992, ApJ, 399, 218
Busso M. et al., 1996, A&A, 311, 253
Deguchi S., 1997, in Lamers H., Habing H. J., eds, IAU Symp. 180, Planetary Nebulae. Kluwer, Dordrecht, p. 151
Draine B. T., Lee H. M., 1984, ApJ, 285, 89
Elitzur M., Ivezić Ž, 2001, MNRAS, submitted
Gilman R. C., 1969, ApJ, 155, L185
Habing H., 1996, A&AR, 7, 97
Habing H. J., Tignon J., Tielens A. G. G. M., 1994, A&A, 286, 523
Harpaz A., Rappaport S., Soker N., 1997, ApJ, 487, 809
Hashimoto O., Izumiura H., Kester D. J. M., Bontekoe Tj. R., 1998, A&A, 329, 213
Hron J., Aringer B., Kerschbaum F., 1997, A&A, 322, 280
Ivezić Ž., Elitzur M., 1995, ApJ, 445, 415 (IE95)
Ivezić Ž., Elitzur M., 1996, MNRS, 279, 1011
Ivezić Ž., Elitzur M., 1997, MNRS, 287, 799 (IE97)
Ivezić Ž., Nenkova M., Elitzur M., 1997, User Manual for DUSTY, Internal Report, Univ. Kentucky, accessible at http://www.pa.uky.edu/~moshe/dusty
Ivezić Ž., Knapp G. R., Elitzur M., 1998, Proc. 6th Annual Conf. of the CFD Society of Canada, June 1998, Québec, pp. IV–13 (astro-ph/9805003)
Ivezić Ž., Knapp G. R., 1998, Proc. IAU Symp. 191 'AGB Stars', August 27–September 1, 1998, Montpelier, France, p. 395 (astro-ph/9812421) (IK98)
Jura M., Kleinmann S. G., 1992, ApJS, 83, 329
Justtanont K., Feuchtgruber H., de Jong T., Cami J., Waters L. B. F. M., Yamamura I., Onaka T., 1998, A&A, 330, L17
Kerschbaum F., Hron J., 1992, A&A, 263, 97
Kerschbaum F., Hron J., 1994, A&AS, 106, 397
Kerschbaum F., Hron J., 1996, A&A, 308, 489
Kerschbaum F., Olofsson H., Hron J., 1996, A&A, 311, 273
Kholopov P. N., Samus N. N., Frolov M. S. et al., 1988, General Catalogue of Variable Stars. 4th edn. 1985 Nauka, Moscow
Knapp G. R., Young K., Lee E., Jorissen A., 1998, ApJS, 117, 209
Knauer T. G., Ivezić Ž., Knapp G. R., 2001, ApJ, submitted
Le Bertre T., 1988a, A&A, 190, 79
Le Bertre T., 1988b, A&A, 203, 85
Lebtzer Th., Hron J., 1999, A&A, 351, 533
Little-Marenin I. R., Little S. J., 1988, ApJ, 333, 305
Little-Marenin I. R., Little S. J., 1990, AJ, 99, 1173
Marengo M., Busso B., Silvestro G., Persi P., Lagage P. O., 1999, A&A, 348, 501 (M99)
Mathis J. S., Rumpl W., Nordsiek K. H., 1977, ApJ, 217, 425
Matsuura M., Yamamura I., Murakami H., Freund M. M., Tanaka M., 1999, A&A, 348, 579
Mattei J. A., Foster G., Hurwitz L. A., Malatesta K. H., Willson L. A., Mennessier M. O., 1997, Proc. ESA Symp. 'Hipparcos – Venice '97', 13–16 May, Venice, Italy, ESA SP-402, pp. 269–274
Mauron N., 1997, Ap&SS, 251, 143
Mauron N., Huggins P. J., 1999, A&A, 349, 203
Netzer N., Elitzur M., 1993, ApJ, 410, 701
Ossenkopf V., Henning Th., Mathis J. S., 1992, A&A, 261, 567
Rowan-Robinson M., Harris S., 1982, MNRAS, 200, 197
Rowan-Robinson M., Harris S., 1983a, MNRAS, 202, 767
Rowan-Robinson M., Harris S., 1983b, MNRAS, 202, 797
Sahai R. et al., 1999, ApJ, 493, 301
Salpeter E. E., 1974a, ApJ, 193, 579
Salpeter E. E., 1974b, ApJ, 193, 585
Sloan G. C., Levan P. D., Little-Marenin I. R., 1996, ApJ, 463, 310
Speck A. K., Barlow M. J., Sylvester R. J., Hofmeister A. M., 2000, A&ASS, 146, 437
Speck A. K., Meixner M., Knapp G. R., 2000, ApJ, 545, L145
van der Veen W. E. C. J., Habing H. J., 1988, A&A, 194, 125
Vassiliadis E., Wood P. R., 1993, ApJ, 413, 641
Whitelock P. A., 1986, MNRAS, 219, 525
Winters J. M., 1998, A&AS, 255, 257

This paper has been typeset from a TEX/LATEX file prepared by the author.

Downloaded from https://academic.oup.com/mnras/article/324/4/1117/1316774 by guest on 21 August 2022